SOLIDIFICATION PROPERTIES OF CERTAIN WAXES AND PARAFFINS

by

JAVIER TORRESOLA

B.S.M.E. Massachusetts Institute of Technology, 1996

Submitted to the Department of Mechanical Engineering
in Partial Fulfillment of
the Requirements for the Degree of

Master of Science
In Mechanical Engineering

at the

MASSACHUSETTS INSTITUTE OF TECHNOLOGY

February 1998

Signature of Author_____
Department of Mechanical Engineering

Certified by_____
Ain A. Sonin
Professor, Mechanical Engineering
Thesis Supervisor

Accepted by_____
Ain A. Sonin
Chairman, Departmental Committee on Graduate Studies
Department of Mechanical Engineering

SOLIDIFICATION PROPERTIES OF CERTAIN WAXES AND PARAFFINS

by

JAVIER TORRESOLA

Submitted to the Department of Mechanical Engineering
On February 5, 1998 in Partial Fulfillment of the
Requirements of the Degree of Master of Science in
Mechanical Engineering

Abstract

Gao and Sonin (1994) have proposed a method for rapid prototyping and microfabrication by precise deposition and solidification of molten microdrops. Objects can be fabricated by a drop-on-demand, computer-controlled droplet generator. To understand the fundamentals of droplet deposition and solidification, experiments have been conducted using microcrystalline wax droplets (Schiaffino and Sonin, 1997a-d).

One of the objectives of this thesis is to determine the solidification properties of the microcrystalline wax and to characterize its solidification. First, we determined the enthalpy and specific heat of the wax as a function of temperature and found that the wax releases latent heat over an extended temperature range, 30-90 °C. Next, we obtained a value for the thermal conductivity of the wax, 0.073 W/m K, by performing a transient solidification experiment and matching the data with the results of a numerical model. These measurements allowed us to formulate a model for characterizing the wax's solidification. In addition, we carried out a general theoretical investigation of solidification of materials that, like wax, release latent heat over a temperature range.

Finally, we performed molten droplet deposition experiments with octacosane, a paraffin with properties similar to those of wax except for its distinct melting point. We were particularly concerned with the contact angles after solidification, which were mostly larger than 90° even at target temperatures close to the melting point. The solidification angle data were compared to those of previous investigators who used waxes in their experiments.

Thesis Supervisor: Dr. Ain A. Sonin
Title: Professor of Mechanical Engineering

ACKNOWLEDGEMENTS

First, I express my deepest gratitude towards my Advisor, Professor Ain A. Sonin. He provided the motivation, guidance and expert advice necessary to make this work a reality. It was a privilege for me to work with such an effective mentor. He is largely responsible for the success of this work.

I would also like to thank my friend and co-worker Mike C. Liu, for his aid in carrying out some of the experiments, creating some of the drawings in this thesis, and suggesting changes to the manuscript. I thank Gregg Duthaler for sharing some research ideas and for his very useful advice. I would like to thank Claire Sasahara and Leslie Regan for their essential administrative help.

The rest of my co-workers at the Fluid Mechanics Laboratory deserve my gratitude for helping me maintain a healthy work-life balance during the past year and a half: Jon, Fred, Carlos, Hugo, Jeremy, Barbara, Erasmo, Cuiling, Nick, Hayden, Guohao, Karen and Darryl. Thanks to all of you.

Lastly, I can never thank my wife, Karem, enough for her unconditional love, patience, and support. She made me want to improve myself every day.

This work was supported by the NSF Graduate Research Fellowship Program, by NSF under grant CTS-9523764 (Division of Chemical and Transport Systems, Program on Fluid, Particulate and Hydraulic Systems), and by NASA under grant NAG 3-1845 (Microgravity Fluid Physics Program).

TABLE OF CONTENTS

LIST OF FIGURES

Chapter 1
INTRODUCTION

Gao and Sonin (1994) have proposed a method for rapid prototyping and microfabrication by precise deposition of molten microdrops. A computer-controlled droplet generator deposits molten microdrops on a subcooled target where they solidify, thereby making it possible to fabricate 3-D objects much like an ink-jet print head generates a 2-D hard copy with ink droplets. Arbitrary shapes can be built with this drop-on-demand fabrication technique.

Dropwise melt deposition has numerous manufacturing applications. For instance, an automated droplet generator would have the precision, speed, and flexibility required in rapid prototyping. Microfabrication is another potential application, particularly if useful engineering materials can be used in a molten microdrop deposition system. Electronics packaging and materials processing are other areas with potential applications for this technology (Gao, 1994; Schiaffino, 1996).

The microdrop deposition process is illustrated in Figure 1.1. The piezo-driven droplet generator ejects a single droplet when a voltage pulse is applied. The droplet then impacts the target, where it solidifies. Pillars are built by depositing molten drops on top of other drops that have already solidified. By moving the droplet generator relative to the target, other shapes can be built. In this process, the shape of any structure depends on the shape that each individual microdrop takes on its target. Therefore, it is essential to understand the dynamic and thermal mechanisms that determine the final shape of each solidified droplet.

When the molten microdrop impacts the target, it initially spreads like a liquid drop on a solid target, driven by capillarity forces. The contact line moves outwards until it reaches a point where it freezes due to heat transfer to the target, and finally the entire droplet solidifies, losing heat to both the ambient air and the solid target.

Schiaffino and Sonin have investigated the deposition and solidification of molten droplets on cold, solid substrates of the same material. They studied in detail the arrest of a molten contact line advancing over a cold solid of the same material (1997a-c).

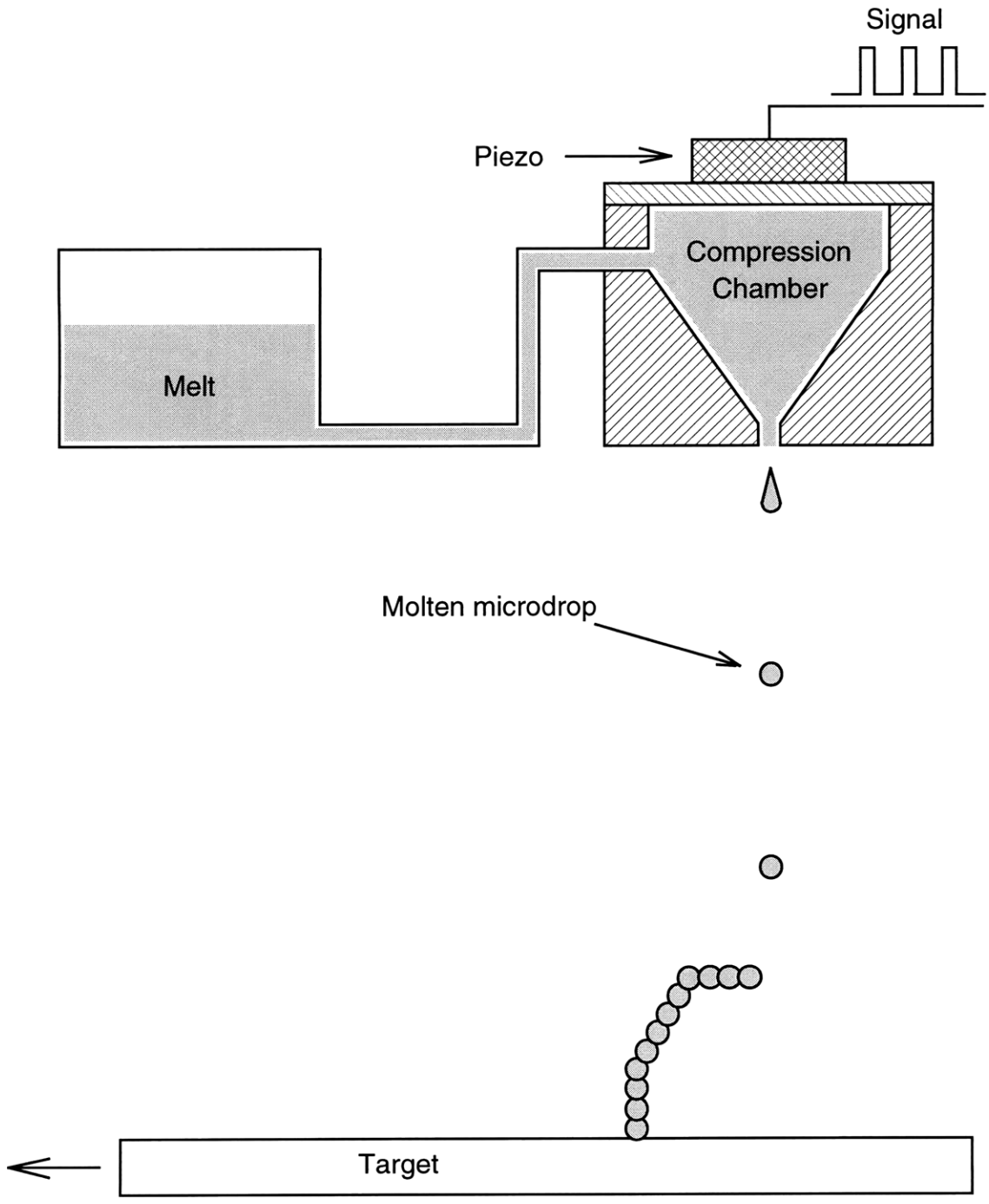

Figure 1.1 Microdrop Delivery System

They developed similarity laws for this process, correlated the data empirically, and proposed a mechanism for the contact line arrest. They also obtained similarity laws for the entire deposition process, and presented a characterization of the deposition process for several different materials (1997d).

The most detailed data of Schiaffino and Sonin pertained to a microcrystalline wax (Reed 6882, made by Reed Wax, Reading MA). Nominal values for the thermal properties of this microcrystalline wax were obtained from its manufacturer and other sources (Warth, 1956). However, accurate values of the wax's specific heat, latent heat, and thermal conductivity were not available. It was also unknown whether the wax's thermal properties accurately reflect the standard model on which Schiaffino and Sonin's similarity laws were based.

Schiaffino and Sonin's model assumed that the wax has a distinct freezing point at which all the latent heat was released. Schiaffino (1996) showed that the microcrystalline wax loses its ability to flow at 90 °C. However, one of the major findings of this thesis is that the wax releases latent heat over an extended temperature range as its temperature falls below 90 °C. This contradicts Schiaffino and Sonin's assumption, implying that their model should be adjusted to reflect the true solidification properties of the wax.

This result, along with the need for knowing the wax's thermal properties, motivated the following objectives of this thesis:

1) to measure the enthalpy, specific heat and thermal conductivity of Reed 6882 microcrystalline wax over a temperature range of 0-115 °C,
2) to establish a model for characterizing solidification of microcrystalline wax,
3) to develop a general model for solidification of materials that release latent heat over a temperature range, and
4) to conduct experiments that study microdrop spreading and solidification using single-component substances that have properties that are similar to those of wax.

Chapter 2

ENTHALPY, SPECIFIC HEAT AND LATENT HEAT OF REED 6882 MICROCRYSTALLINE WAX

2.1 Objectives

The main objectives in this experiment were to determine the enthalpy of Reed 6882 microcrystalline wax over a temperature range of 0-115 °C, and to establish a model for characterizing its solidification or melting. Preliminary experiments showed that, while the wax appears to lose its ability to flow at 90 °C (Schiaffino, 1996), it releases latent heat over an extended temperature range as its temperature falls below 90 °C. The enthalpy of the wax as a function of temperature was measured by dropping the wax inside a thermos that contained water at a different temperature, and recording the final equilibrium temperature.

2.2 Apparatus and its calibration

There are several methods documented in the literature for measuring the calorimetric properties of a substance. The most common are Differential Thermal Analysis (DTA), Differential Scanning Calorimetry (DSC), adiabatic calorimetry, and the drop method (Wendlandt, 1986; Mathot, 1984; Landolt-Bornstein, 1995a). Adiabatic calorimetry is the most accurate method available. DTA and DSC have the advantage that only one experiment yields the enthalpy of a substance as a function of temperature. However, the equipment required for DTA, DSC, and adiabatic calorimetry is expensive compared to the drop method. We chose to use a variation of the drop method since it is inexpensive, simple and has adequate accuracy (as low as 1%).

The calorimetric experiments were carried out inside a thermos, shown in Figure 2.1. A laboratory oven and a hot plate were used for heating the wax samples. In some experimental trials, the wax sample was wrapped in aluminum foil for better handling.

The first step was to determine the effective heat capacity of the thermos, C_t, which is a function of the volume of fluid inside it. This calibration procedure was very similar to the subsequent experiments with wax, with the exception that ice was used instead of wax. The procedure consisted of pouring a certain amount of cold water into

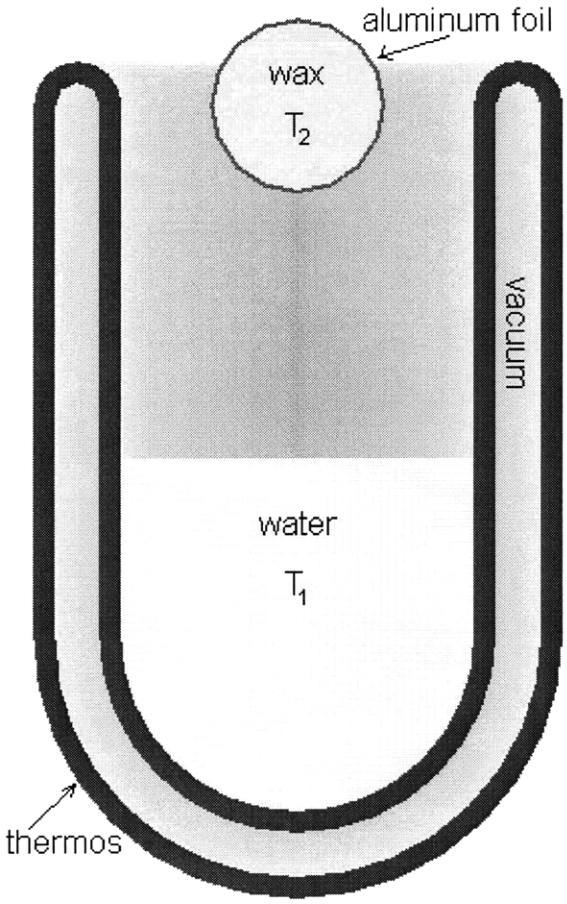

Figure 2.1 Apparatus for Wax Enthalpy Experiment

the thermos, measuring its temperature inside the thermos, and then dropping into it an ice cube, initially at 0 °C. After the ice melted and thermal equilibrium was reached, the final temperature inside the thermos was measured. Since the specific heat and the latent heat of water are well known, and since we measured both the mass of the water and that of the ice cube initially, the heat capacity of the thermos could be determined from the first law of thermodynamics (see Equation 2.1 below). The procedure was repeated at different initial water temperatures and different initial amounts of water inside the thermos.

The first law of thermodynamics gives the following expression for the heat capacity of the thermos, C_t in our calibration experiment:

$$C_t = \frac{m_{ice}\,(L + c_{water}(T_e - T_f)) - Q_{12}}{(T_1 - T_e)} - m_{water}c_{water}\ , \qquad (2.1)$$

where m_{ice} is the mass of the ice cube, m_{water} and T_1 are the mass and temperature of the water initially inside the thermos, L and c_{water} are the latent heat and specific heat of water, respectively, T_f is the fusion point of water, T_e is the final equilibrium temperature inside the thermos, and Q_{12} is the heat loss to the ambient. The heat loss to the ambient was determined to be less than 10 J, which was much smaller than the heat transferred to the water, and therefore Q_{12} was neglected in all calculations.

2.3 Methods

The next step was to perform the actual experiments that would determine the calorimetric properties of the wax over a temperature range of 0-115 °C. Three slightly different methods were used. The simplest method was used when the wax was initially in a liquid state (temperature above 90 °C). The thermos contained water at room temperature initially and then molten wax would be poured from a beaker. We measured the initial temperature of the water inside the thermos, T_1, as well as the initial temperature of the wax, T_2 (see Figure 2.1). After the wax was poured, we waited for thermal equilibrium to take place inside the thermos, and then the final equilibrium temperature, T_e, was measured. Both the mass of the water, m_{water}, and that of the wax, m_{wax}, were measured beforehand.

A slightly different procedure was used for the trials in which the initial wax temperature was between 40-90 °C. In this case, the wax sample was heated inside an oven and it was enclosed in aluminum foil. The foil allowed for better handling of the wax as it was transferred from the oven to the thermos. The wax and foil were then dropped into the thermos and mixed with water as before.

In both procedures, the enthalpy decrease of the wax, $\Delta H = H(T_2) - H(T_e)$, was determined using the following equation:

$$\Delta H = \frac{(m_{water}c_{water} + C_t)\cdot(T_e - T_1) - m_{foil}c_{foil}(T_2 - T_e)}{m_{wax}}\ , \qquad (2.2)$$

where m_{wax} is the mass of the wax, T_2 is the initial temperature of the wax, m_{foil} is the mass of the aluminum foil, if any, and c_{foil} is the specific heat of the aluminum foil. The other quantities are as defined in Equation 2.1. The effective heat capacity of the thermos, C_t, is a linear function of the height of water in contact with the thermos' walls. The value of this function was estimated by interpolating the calibration measurements.

A third procedure was necessary in order to determine the enthalpy changes of the wax at lower temperatures. This time the wax was initially inside the thermos, surrounded by cold water to ensure temperature uniformity in the wax. Then warm water was poured inside the thermos and the final equilibrium temperature was measured as before.

For this case, a slightly different expression applies:

$$\Delta H = \frac{m_3 c_{water}(T_3 - T_e) - (m_1 c_{water} + C_t)\cdot(T_e - T_2)}{m_{wax}}, \qquad (2.3)$$

where m_3 and T_3 are the mass and temperature of the warm water initially outside the thermos, respectively, and m_1 is the mass of the cold water initially inside the thermos with the wax. T_2 is the temperature of both the water and the wax initially inside the thermos.

The enthalpy values obtained from the individual measurements were adjusted so that each measurement would give the enthalpy decrease from the initial wax temperature, T_2, to a fixed reference temperature, T_{ref} = 13.5 °C. The adjusted enthalpy change, ΔH^*, that the wax undergoes from T_{ref} to T_2 is given by:

$$\Delta H^* = \Delta H + (T_e - T_{ref})\cdot c_{wax}\,|_{T_{ref}}, \qquad (2.4)$$

where $c_{wax}\,|_{T_{ref}}$ is the measured specific heat of the wax at 13.5 °C and ΔH is given by either Equation 2.2 or Equation 2.3. The experiments were designed in such a way that the final temperature of the wax, T_e, was always within 5 °C of the reference temperature. Therefore, the error introduced by the adjustment remained small. The specific heat of the wax near 13.5 °C did not appear to have a large temperature dependence and its measured value was 2000 ± 10% J/kg K.

2.4 Results

The calibration measurements showed a linear relationship between the effective heat capacity of the thermos and the mass of water inside of it. Figure 2.2 shows the data points, as well as the interpolation curve, C_t = 189m + 64, where m is the final mass inside the thermos, in kg, and C_t is given in kJ/kg.

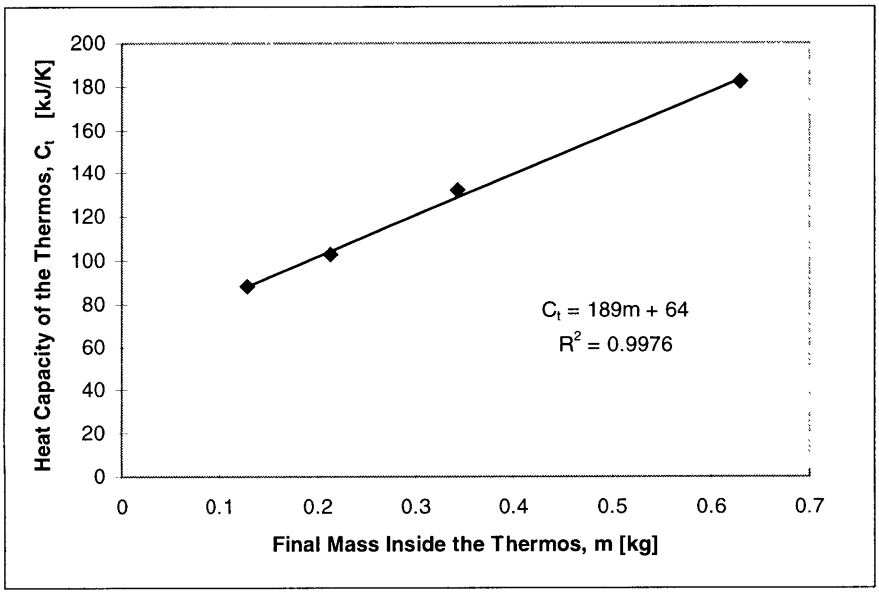

Figure 2.2 Heat Capacity of Thermos vs. Final Mass of Water

Figure 2.3 shows the wax's enthalpy increase when the temperature increases from the reference temperature, 13.5 °C, to T_2 (°C). The measurements are fitted with the following curve:

$$T_2 < 90\ ^\circ\text{C}, \quad \Delta H^* = -27.6 + 2.08T_2 - 0.0104T_2^{\,2} + 0.000364T_2^{\,3} \ \text{[kJ/kg]}$$
$$T_2 > 90\ ^\circ\text{C}, \quad \Delta H^* = 81.2 + 2.89T_2 \ \text{[kJ/kg]} \qquad (2.5)$$

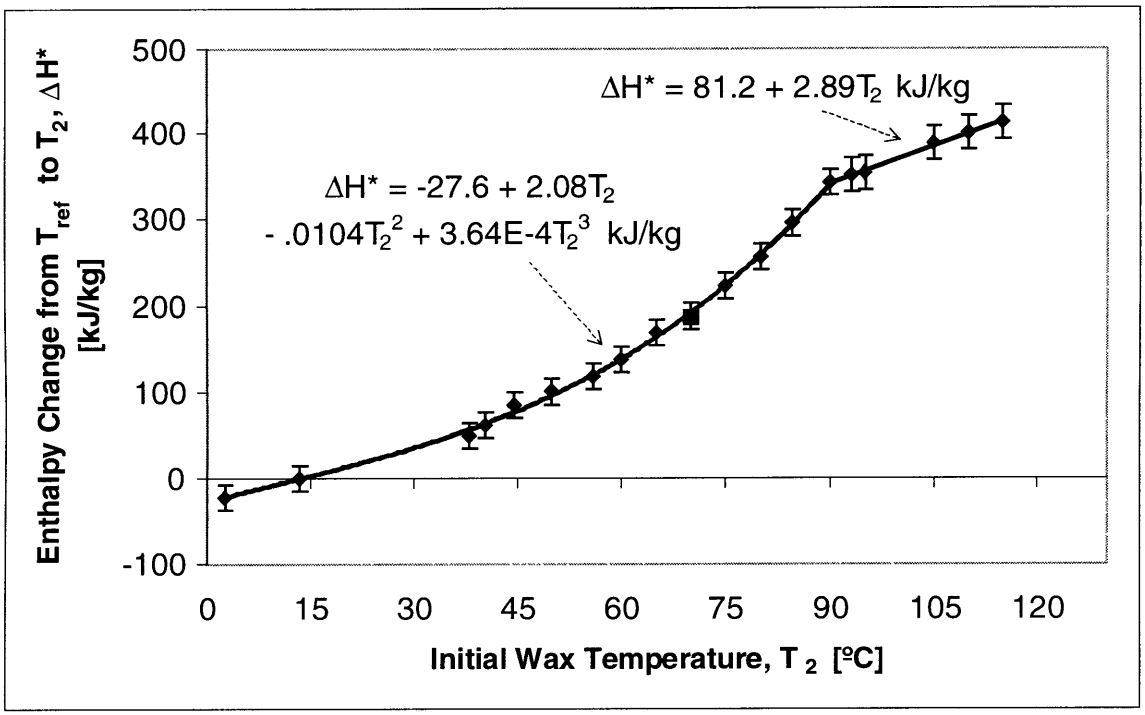

Figure 2.3 Enthalpy Change of Wax vs. Initial Temperature

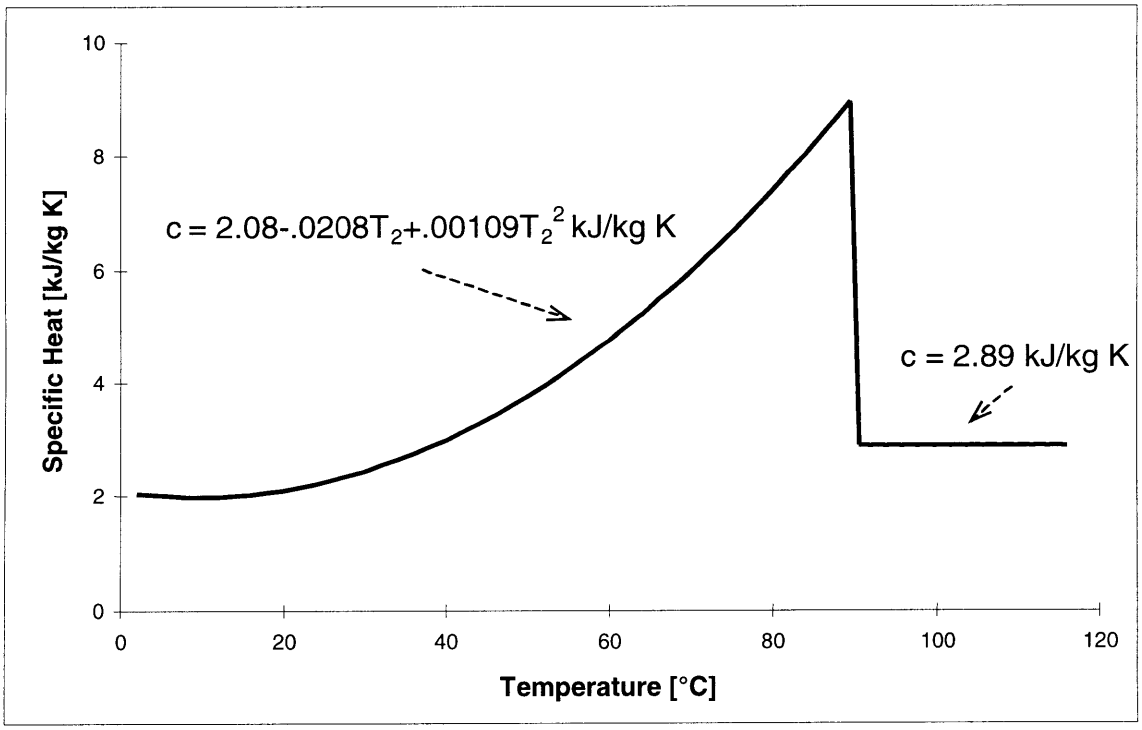

Figure 2.4 Specific Heat of Wax vs. Temperature

Equation 2.5 can be differentiated with respect to T_2 to obtain an expression for the specific heat as a function of temperature (see Figure 2.4 above):

$$T_2 < 90\ °C, \quad c = 2.08 - .0208T_2 + .00109T_2^2 \ \text{[kJ/kg K]}$$
$$T_2 > 90\ °C, \quad c = 2.89 \ \text{[kJ/kg K]} \tag{2.6}$$

The latent heat of the wax, L, can be defined as the area under the curve of Figure 2.4 (in the transition region) that is also above a "baseline" specific heat, which we will take to be 2000 J/kg K, the specific heat below 30 °C.

i.e.
$$L = \int_{30°C}^{90°C} [c(T) - 2000\ J/kgK]\,dT \tag{2.7}$$

Based on this definition, the latent heat of the microcrystalline wax is 190 ± 5% kJ/kg.

2.5 Conclusions

The experiments indicate that, at temperatures between 0 °C and 115 °C, the enthalpy of the 6882 microcrystalline wax can be represented as varying linearly with temperature in two regimes: when its temperature is either below 30 °C (solid) or above 90 °C (liquid). Between 30 °C and 90 °C, the wax goes through a "mushy zone", much like an alloy, where latent heat is released as it cools (Lipton et al., 1982). In the solid state below 30 °C, the specific heat of wax is 2000 ± 10% J/kg K. The liquid state above 90 °C has a higher specific heat, 2900 ± 5% J/kg K. The latent heat released between 90 °C and 30 °C, taking 2000 J/kg K as the baseline specific heat, is 190 ± 5% kJ/kg.

Chapter 3

TRANSIENT SOLIDIFICATION OF MICROCRYSTALLINE WAX: EXPERIMENTS, THEORY, THERMAL CONDUCTIVITY

One of our primary concerns is to understand the solidification process of wax. The enthalpy experiment revealed that wax releases latent heat over a temperature range as it solidifies, which is caused by the fact that wax is composed of multiple hydrocarbons with different fusion points. Therefore, solidification of wax occurs differently from that of single-component substances that have a distinct melting point. We have designed an experiment to measure the temperature distribution during solidification of wax under one-dimensional conduction.

The experimental apparatus, shown in Figure 3.1, is very similar to that used by Garcia and Prates (1978) to characterize solidification in metals. It consists of a Plexiglas cylinder, containing the wax, insulated on all sides except the bottom, which is water-cooled. A thin copper plate separates the wax inside the cylinder from the water jet. Three thermocouples were placed inside the wax at different heights from the copper plate in order to measure the temperature distribution in the wax during solidification. The distance from the thermocouples to the copper plate was small compared to the total height of the wax and the radius of the plate. This allowed us to assume one-dimensional heat transfer in a semi-infinite body. A fourth thermocouple was attached to the copper plate.

The wax was initially inside the container and everything was heated inside an oven to a temperature T_o above the melting point of the wax (90 °C). At time t = 0, the apparatus was removed from the oven and the water jet, at about 20 °C, was turned on. The temperature of the wax was recorded as a function of time at the three different heights and the temperature of the copper plate, T_c, was recorded as well.

A model was devised to characterize the transient solidification process, using the following assumptions:

1. Purely conductive, one-dimensional heat transfer (convection in the liquid was neglected).
2. The wax is treated as a semi-infinite body.

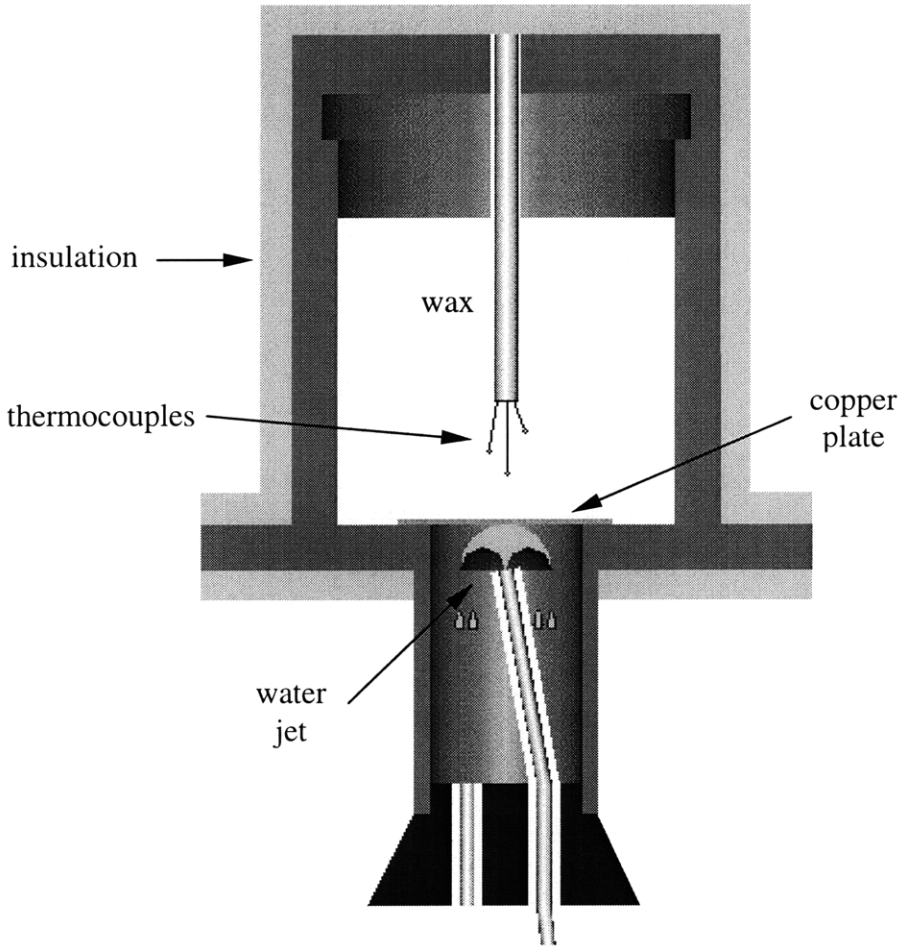

Figure 3.1 Apparatus for Wax Solidification Experiment

3. The temperature at the boundary, T_c, is given and it is equal to the measured temperature of the copper plate.
4. The density, ρ, of wax below 90 °C is 930 kg/m^3 (the value measured at 20 °C) and above 90 °C, it is equal to 780 kg/m^3 (as measured at 95 °C).

i.e.
$$\rho = 930 \text{ kg/m}^3 \qquad T < 90 \text{ °C}$$
$$\rho = 780 \text{ kg/m}^3 \qquad T > 90 \text{ °C} \tag{3.1}$$

5. The specific heat, c, of wax is a function of its temperature and it is given by Eq. 2.6.
6. The thermal conductivity, k, of wax (unknown) is independent of temperature.

The energy equation for one-dimensional transient conduction gives:

$$\frac{\rho(T)\cdot c(T)}{k}\cdot\frac{\partial T}{\partial t}=\frac{\partial^2 T}{\partial x^2}\ , \tag{3.2}$$

where x is the vertical distance from the cooling plate and T is the temperature. Both the density and the specific heat of wax are dependent on temperature. The boundary and initial conditions for the semi-infinite body approximation are:

$$\begin{aligned} &x = 0: \quad T = T_c \\ &x \rightarrow \infty: \quad T = T_o \\ &t = 0: \quad T = T_o \end{aligned} \tag{3.3}$$

The energy equation was solved numerically, using the following explicit finite-difference approximation:

$$\frac{\rho(T_i^n)\cdot c(T_i^n)}{k}\cdot\frac{T_i^{n+1}-T_i^n}{\Delta t}=\frac{T_{i+1}^n+T_{i-1}^n-2T_i^n}{\Delta x^2}\ , \tag{3.4}$$

where Δx is the grid size, Δt is the time step, the subscript i denotes the space discretization, and the superscript n represents the time discretization. The temperature field at the time level n+1 can be calculated explicitly from Equation 3.4 if the temperature field at time n is known. Using the initial and boundary conditions (Equation 3.3) along with Equation 3.4, we can compute the temperature field of the wax as a function of time.

The only difficulty that prevented the model described above from predicting transient solidification in wax is that the thermal conductivity of wax remained unknown. However, using our model in conjunction with the solidification experiments, we can iteratively find a value for the thermal conductivity that makes the numerical model agree with the experimental data. The experiment will serve as an indirect measurement of the thermal conductivity of wax.

Figure 3.2 shows the values of the thermal conductivity that make the numerical model agree with the experimental trials. Each trial gave three different estimates of the thermal conductivity, one for each thermocouple in the wax. There was no significant correlation between the height of the measuring thermocouple and the resulting thermal conductivity, indicating that the model is accurate. The average value obtained for the thermal conductivity was:

$$k = 0.073 \text{ W/m K.} \tag{3.5}$$

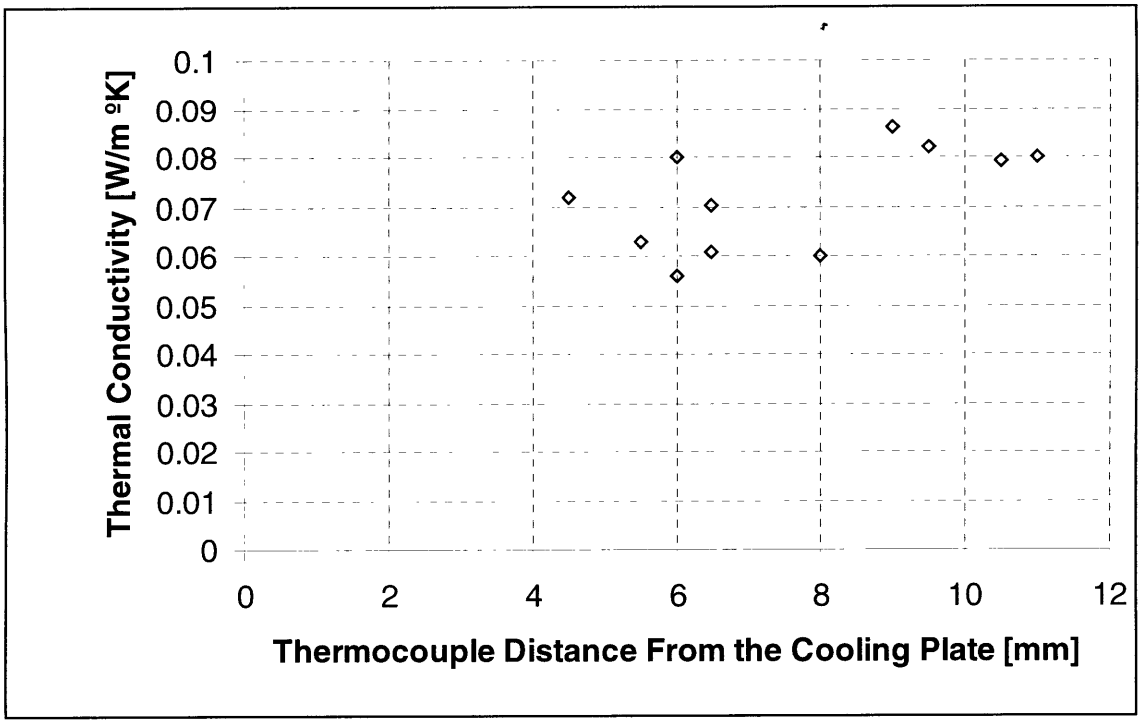

Figure 3.2 Thermal Conductivity vs. Distance between Thermocouple and Copper Plate

Accounting for the scatter of the data, ± 20%, and allowing for a 10% systematic error due primarily to our simplifying assumptions, the accuracy of the measurement is ± 30%.

It can be shown (see Appendix A) that if we keep track of the point where the wax has a given temperature, say 90 °C, as it moves away from the cooling plate, the vertical distance between that point and the plate is proportional to the square root of time. This is true even though Equation 3.2 is non-linear, as long as the temperature of the cooling plate is constant and the semi-infinite body assumption holds. Both our numerical model and the experiments show the square root of time dependence of the solidification front, as shown in Figure 3.3.

The temperature history at the three different distances from the plate is shown in Figure 3.4 for one trial. The results given by the numerical model are also shown in the chart. Three different values of the thermal conductivity were used for the three different thermocouple heights. By using the proper thermal conductivity, the experimental temperature history curve can also be predicted accurately.

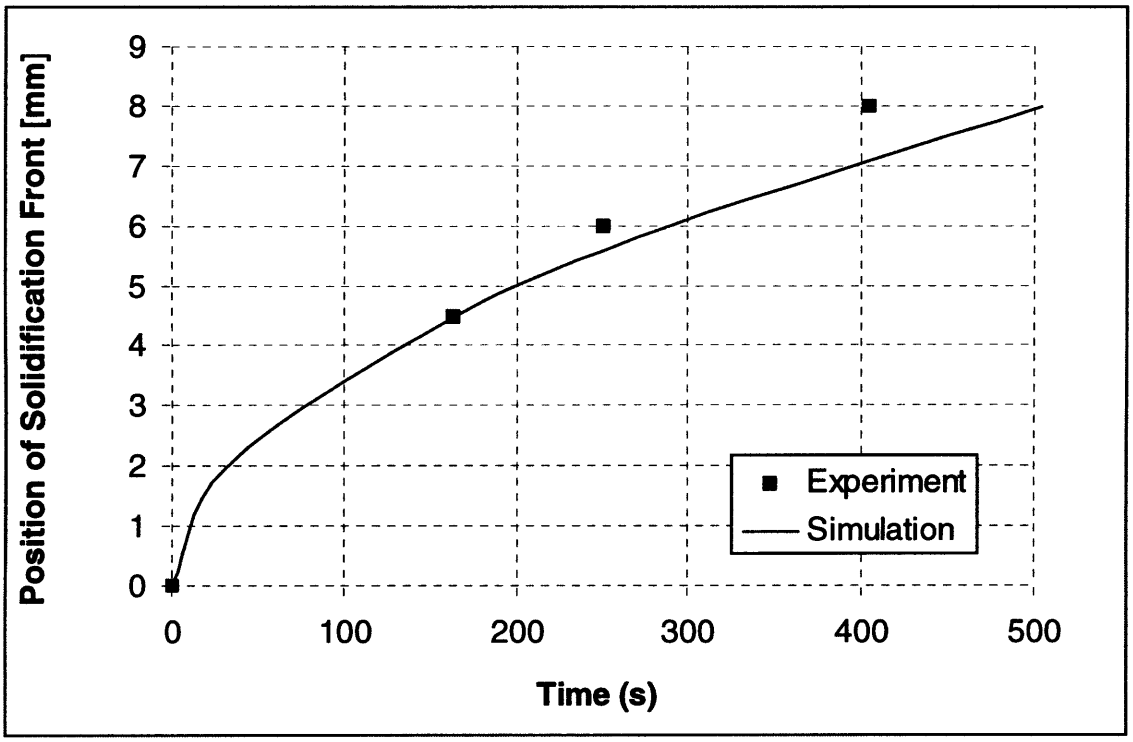

Figure 3.3 Position of Solidification Front (T=90 °C) vs. Time

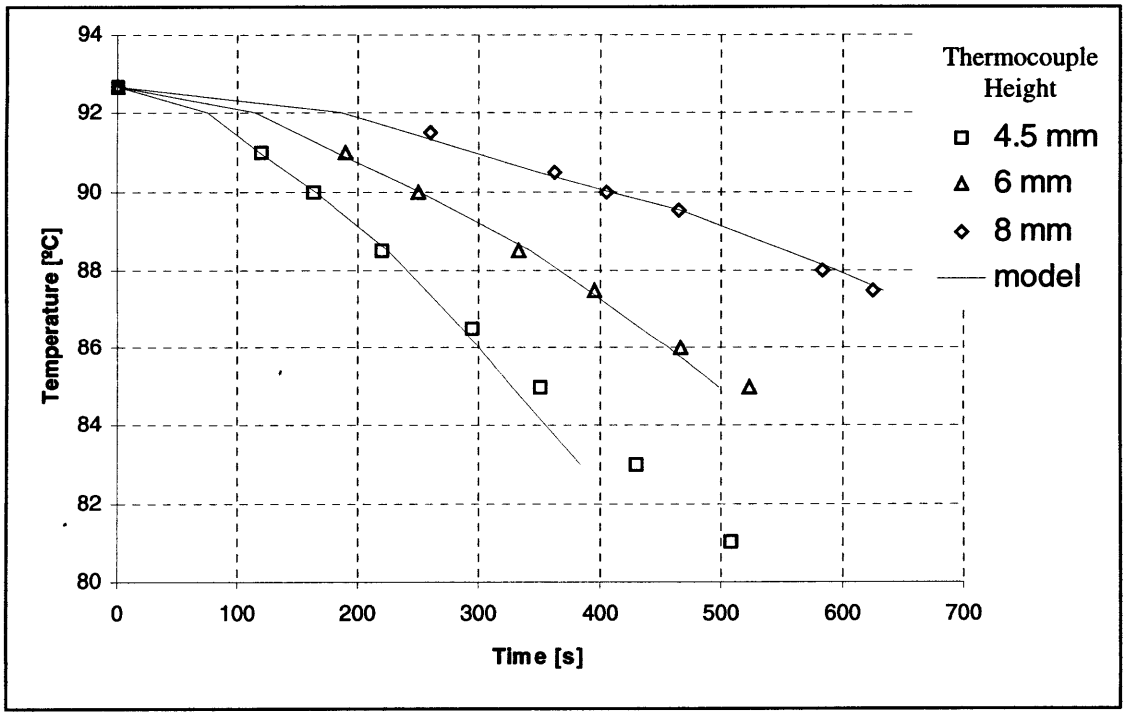

Figure 3.4 Temperature History

The experiment provided us with a better understanding of the solidification process in wax. The measurement of the wax's thermal conductivity, approximately 0.07 W/m K, is a very important result. By using this value for the thermal conductivity, along with the measured specific heat curve given by Equation 2.6 and the measured densities of solid and liquid wax, we can predict transient conduction in the wax. The temperature histories given by the experiment and the numerical model agreed, thus confirming the validity of our enthalpy measurements.

Chapter 4

THEORETICAL INVESTIGATION OF SOLIDIFICATION OF A CLASS OF MATERIALS WITH TEMPERATURE-DEPENDENT SPECIFIC HEAT

In Chapter 2, we determined the enthalpy of wax as a function of temperature. The experiment revealed that wax releases latent heat over a temperature range as its temperature falls below 90 °C. This result has increased our interest in studying the solidification process in materials with an enthalpy curve similar to that of wax. Our goal is to determine the parameters that control the solidification rate in such materials.

We decided to study a simple problem, solidification of a semi-infinite body under one-dimensional conduction. This is essentially the same problem studied in Chapter 3, with slightly different assumptions about the material properties. For simplicity, we assumed that both the density, ρ, and the thermal conductivity, k, of the material are constant. The specific heat of the material is given by the curve shown in Figure 4.1. The material has the same specific heat, c_o, in the completely solid and liquid phases. Beginning at a temperature T_s, the specific heat increases linearly with temperature, reaching a peak at temperature T_f, and falling to its original value, c_o, for temperatures above T_f. The latent heat, L, is equal to the shaded area.

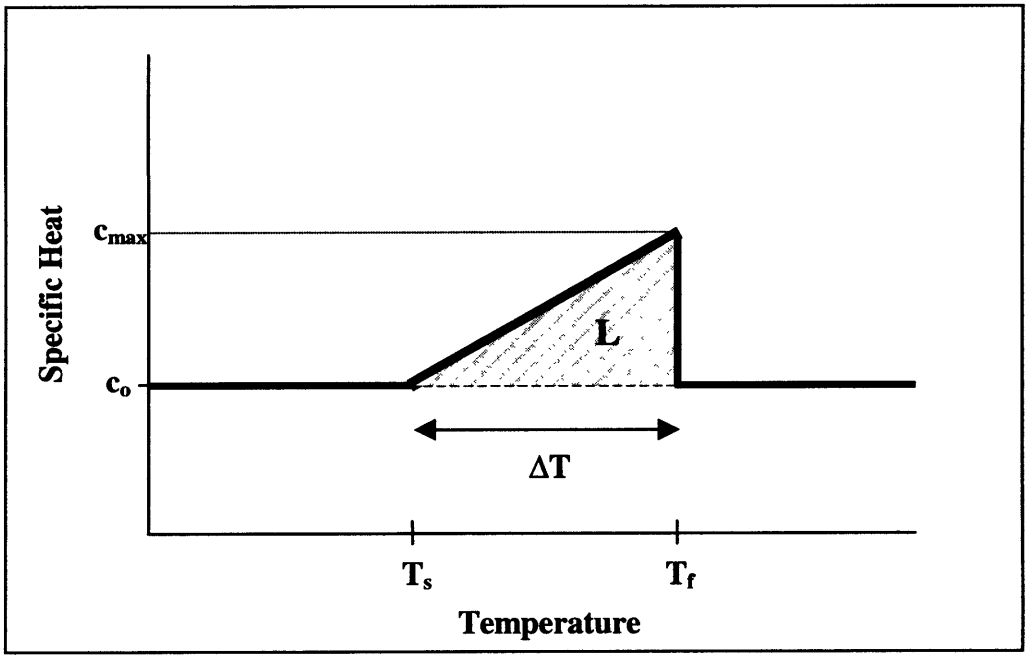

Figure 4.1 Specific Heat as a Function of Temperature

The underlying reason for choosing this particular profile in the melting transition zone is that it is similar to the measured specific heat curve for microcrystalline wax (Figure 2.4). In this case, however, the specific heat of the completely solid region is taken for simplicity to be the same as that of the liquid phase. The size of the transition zone, T_f - T_s, is hereafter referred to as ΔT. The maximum specific heat is

$$c_{\max} = \frac{2L}{\Delta T} + c_o . \tag{4.1}$$

In order to track the solidification front, one has to define a fusion temperature. Since it is at 90 °C that the wax loses its ability to flow (Schiaffino 1996), we have defined 90 °C as the fusion point. In the measured specific heat curve for wax, 90 °C corresponds to T_f in Figure 4.1.

One-dimensional solidification in materials that release latent heat at a distinct melting point is a well-understood process. Carslaw and Jaeger (1959) give an analytical solution for one-dimensional solidification in a semi-infinite liquid body, initially at a temperature T_o, which is suddenly exposed to a temperature $T_c < T_f$ at x = 0. The position of the solidification front, x_s, is given by

$$x_s = \lambda\sqrt{\alpha t} , \tag{4.2}$$

where α is the thermal diffusivity of the material, t is the time, and λ is a "solidification coefficient" which is a function of two other parameters, the superheat,

$$\beta = \frac{T_o - T_f}{T_f - T_c} , \tag{4.3}$$

and the Stefan number,

$$S = \frac{c_o (T_f - T_c)}{L} . \tag{4.4}$$

We will attempt to solve the problem described above, although this time for a material with the specific heat curve given by Figure 4.1. It can be shown (see Appendix A) that even for this kind of material, the position of the solidification front still has the form:

$$x_s = \lambda\sqrt{\alpha_o t} , \tag{4.5}$$

where

$$\alpha_o = \frac{k}{\rho c_o}, \tag{4.6}$$

and c_o is given in Figure 4.1. It is our goal to determine what parameters the solidification coefficient, λ, depends on.

Based on dimensional analysis (see Appendix A), the solidification coefficient for this kind of material still depends on the superheat, β, and the Stefan number, $S = c_o(T_f - T_c)/L$. However, because latent heat is released over a temperature range, we need to introduce an additional parameter. This parameter can be expressed in dimensionless form as $\Delta T/(T_f - T_c)$. Consequently,

$$\lambda = \lambda\left(\beta, S, \frac{\Delta T}{(T_f - T_c)}\right). \tag{4.7}$$

Knowing the parameters that determine the solidification coefficient, the next step is to characterize the function itself by varying the three input parameters and computing the value of λ. We were able to do this by using a numerical model nearly identical to the one described in Chapter 3. The only differences between the model in Chapter 3 and the one used for computing λ are the assumptions regarding the properties of the material. The model solves the energy equation

$$\frac{\rho \cdot c(T)}{k} \cdot \frac{\partial T}{\partial t} = \frac{\partial^2 T}{\partial x^2}, \tag{4.8}$$

with initial and boundary conditions

$$\begin{aligned} &x = 0: \quad T = T_c, \\ &x \rightarrow \infty: \quad T = T_o, \\ &t = 0: \quad T = T_o, \end{aligned} \tag{4.9}$$

using the finite-difference approximation

$$\frac{\rho \cdot c(T_t^n)}{k} \cdot \frac{T_t^{n+1} - T_t^n}{\Delta t} = \frac{T_{t+1}^n + T_{t-1}^n - 2T_t^n}{\Delta x^2}. \tag{4.10}$$

Equation 4.10 was solved to obtain the temperature field as a function of time. The position of the solidification front at any given time was determined by tracking the location of temperature T_f in the wax. The value of the solidification coefficient, λ, was then calculated from Equation 4.5.

The initial and boundary conditions, along with the values of c_o, L and ΔT in the specific heat curve (Figure 4.1) determine the values of β, S, and $\Delta T/(T_f - T_c)$ in Equation 4.7. We solved the energy equation numerically for different values of the three dimensionless parameters and recorded the resulting solidification coefficient, λ, for each combination of β, S, and $\Delta T/(T_f - T_c)$. Figures 4.2 and 4.3 show the dependence of the solidification coefficient on S and $\Delta T/(T_f - T_c)$, for $\beta = 0.0556$ and $\beta = 0.111$.

When the Stefan number is very small, the solidification coefficient approaches zero. The solidification coefficient increases with the Stefan number, approaching a maximum value which occurs at large Stefan numbers and depends on the superheat, β. Increasing $\Delta T/(T_f - T_c)$ also increases the solidification coefficient, again up to the same maximum value that depends on β. The maximum value for the solidification coefficient corresponds to the classic problem of transient conduction in a semi-infinite body, where the specific heat of the material is constant (i.e. the latent heat is negligible). This maximum value was 2.74 for $\beta = 0.0556$ and 2.33 for $\beta = 0.111$.

When $\Delta T/(T_f - T_c)$ is very small, the solidification coefficient approaches the solution given by Carslaw and Jaeger (1959) for materials that release latent heat at a distinct melting point. This solution is represented by the curve $\Delta T/(T_f - T_c) = 0$ in Figures 4.2 and 4.3.

By comparing Figures 4.2 and 4.3, we reach the expected conclusion that the larger the superheat, the smaller the solidification coefficient. Thus, the solidification front takes longer to reach any given location in the wax.

Another interesting way of looking at the results can be achieved if we change the form of one of the dimensionless parameters that the solidification coefficient depends on. If we multiply the Stefan number, $c_o(T_f - T_c)/L$, times $\Delta T/(T_f - T_c)$, we get $c_o\Delta T/L$. Therefore, we can rewrite Equation 4.7 as

$$\lambda = \lambda\left(\beta, \frac{c_o \Delta T}{L}, \frac{\Delta T}{(T_f - T_c)}\right). \tag{4.11}$$

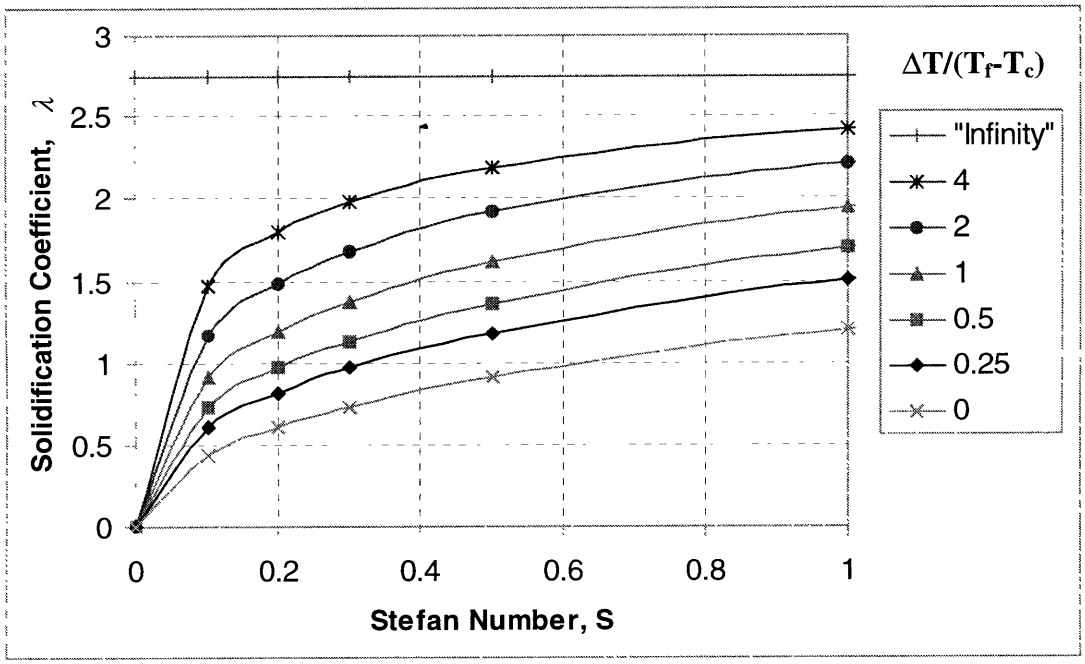

Figure 4.2 Dimensionless Solidification Coefficient as a function of $\Delta T/(T_f - T_c)$ and the Stefan Number; $\beta = 0.0556$

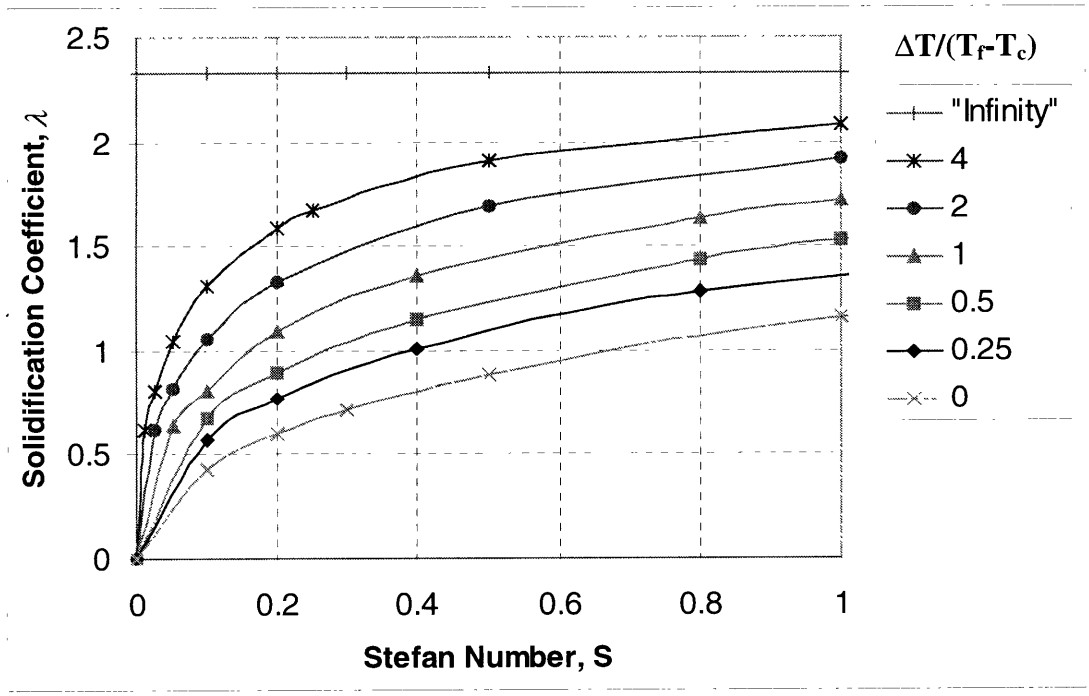

Figure 4.3 Dimensionless Solidification Coefficient as a function of $\Delta T/(T_f - T_c)$ and the Stefan Number; $\beta = 0.111$

Figures 4.4 and 4.5 show the solidification coefficient as a function of $c_o\Delta T/L$ and $\Delta T/(T_f - T_c)$, again for two different values of β. An interesting observation is that if $\Delta T/(T_f - T_c)$ is sufficiently large, then the dependence of the solidification coefficient on $\Delta T/(T_f - T_c)$ becomes very weak. Therefore, we can say that for $\Delta T/(T_f - T_c)$ greater than, say 0.5,

$$\lambda \approx \lambda\left(\beta, \frac{c_o \Delta T}{L}\right). \tag{4.12}$$

Furthermore, since all three quantities in $c_o\Delta T/L$ are material properties, we can say that for a given material, for $\Delta T/(T_f - T_c) > 0.5$,

$$\lambda \approx \lambda(\beta). \tag{4.13}$$

This is a very useful result that simplifies the analysis of solidification in materials with a large transition zone.

The numerical simulations proved to be effective in determining how various parameters affect solidification in materials that, like wax, release latent heat over a temperature range. We have learned how solidification in materials of this kind differs from solidification in materials that have a distinct melting point. The general result is that, for two materials with the same latent heat, solidification occurs faster in the material with the larger range over which latent heat is released.

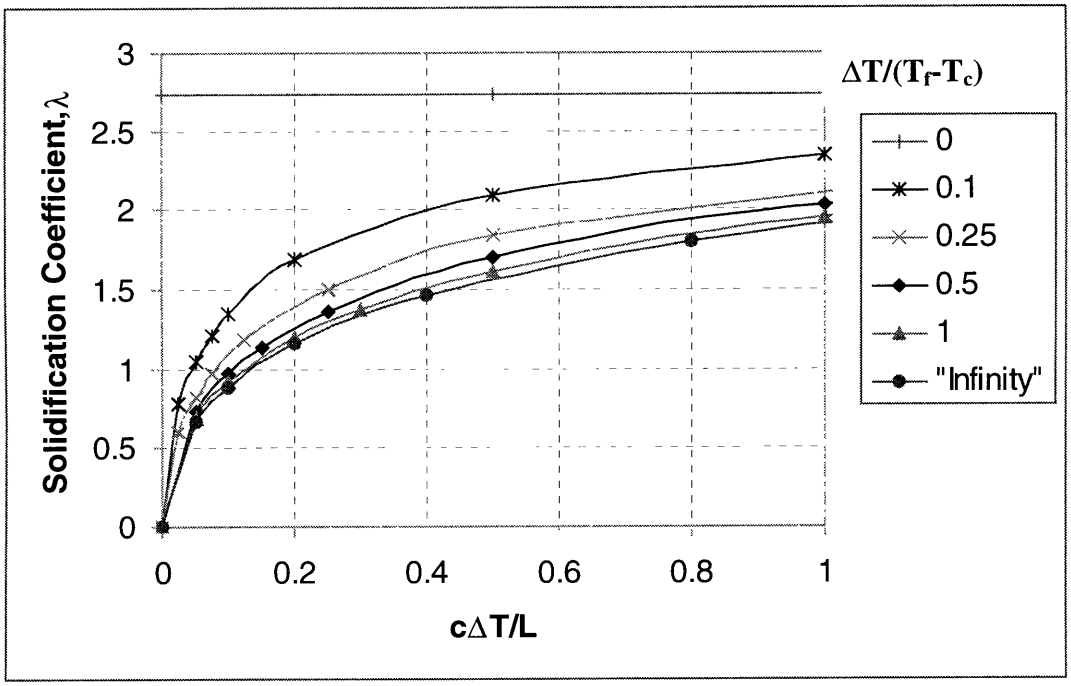

Figure 4.4 Dimensionless Solidification Coefficient as a function of $\Delta T/(T_f-T_c)$ and $c_o\Delta T/L$; $\beta = 0.0556$

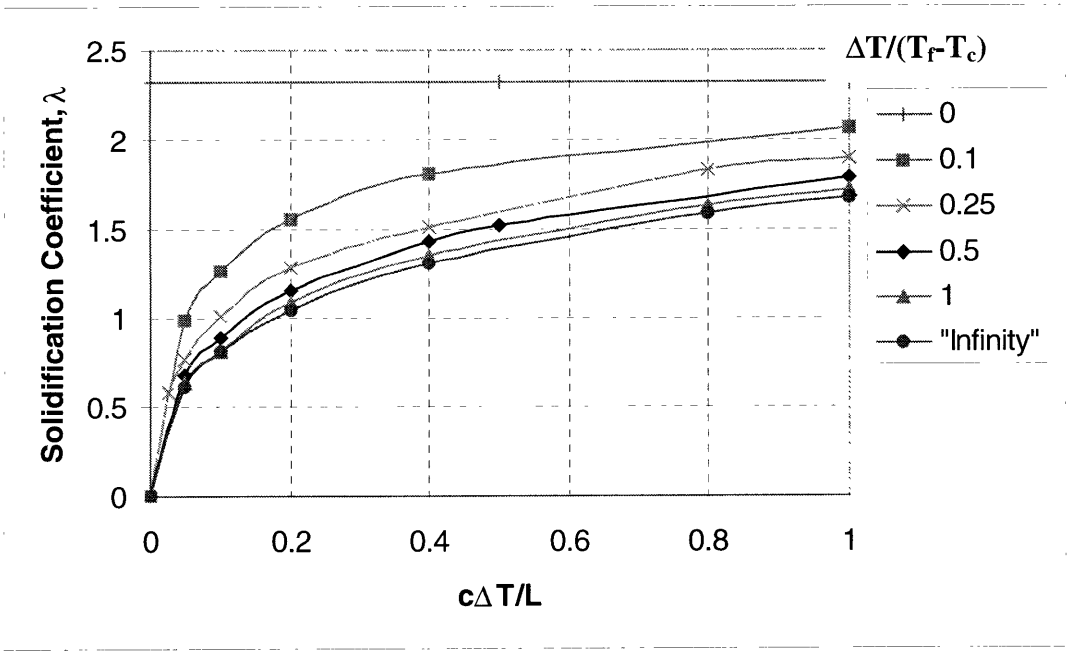

Figure 4.5 Dimensionless Solidification Coefficient as a function of $\Delta T/(T_f-T_c)$ and $c_o\Delta T/L$; $\beta = 0.111$

Chapter 5

DEPOSITION OF MOLTEN OCTACOSANE DROPLETS: SOLIDIFICATION ANGLES

5.1 Introduction

In dropwise melt deposition, the post-solidification contact angle of each deposited microdrop on its target is an important parameter that determines the final shape of each drop. Operating with waxes, Gao and Sonin (1994), Gao (1994), Schiaffino (1996) and Schiaffino and Sonin (1997b) investigated the dependence of the solidification angle, θ_s, on the delivery and thermal conditions. The solidification angle is defined as in Figure 5.1. Schiaffino and Sonin (1997b) showed that for wax droplets spreading on a cold solid of the same material, θ_s is essentially dependent only on the Stefan number, S. It is desired to extend their work by using different materials.

Paraffins, defined as hydrocarbons with molecular formula C_nH_{2n+2}, have thermo-physical properties similar to those of wax. However, since paraffins are single-component substances, they have sharp transition points, unlike waxes, which have multiple components. These characteristics increased our interest for using paraffins in our microdrop deposition experiments.

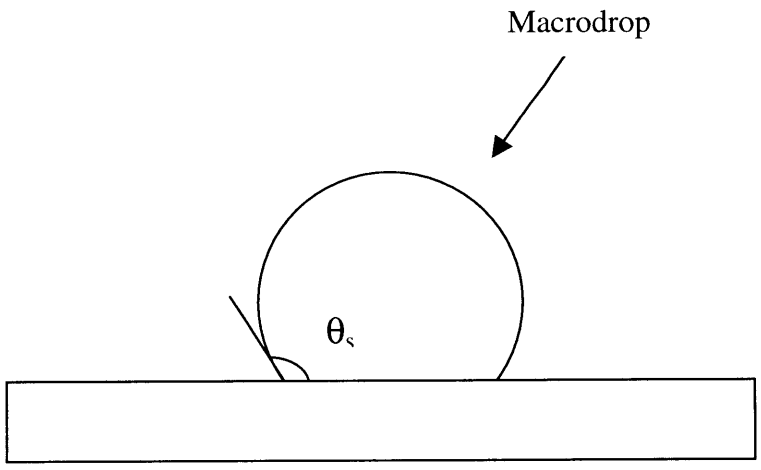

Figure 5.1 Droplet Solidification Angle

Octacosane ($C_{28}H_{58}$) is a paraffin with a fusion point of 61°C. Its thermo-physical properties are well documented in the literature and are listed in Appendix B. We studied the process of spreading and arrest of octacosane drops, in particular the solidification angles.

5.2 Experimental Apparatus

Figure 5.2 depicts the experimental apparatus used for depositing microdrops, and at the same time, visualizing and recording the deposition process. Droplets of molten octacosane, approximately 50 μm in diameter, are delivered from the same droplet generator as the one used by Gao (1994) and Schiaffino (1996), to a flat octacosane target, where they spread and solidify. The entire process is monitored and recorded using microscope lenses fitted to a CCD video camera, which sends the video signal to a monitor and a SVHS recorder.

The droplet generator is a piezo-driven, adapted commercial ink-jet print head (Dataproducts SI320). It has 32 nozzles, 50 μm in diameter, each of which can be independently fired by applying voltage pulses to the piezoelectric transducers. Temperature controllers and heaters regulate both the target temperature and the temperature of the nozzles in the droplet generator. A pulse generator (HP-214B) controls the amplitude, frequency and width of the voltage pulses. A calibrated crosshair generator is used for measuring droplet dimensions.

5.3 Experiments with Continuously Fed Macrodrops

Gao (1994) and Schiaffino (1996) used an innovative technique for studying contact line motion and arrest. It consists of operating the droplet generator at a frequency high enough that droplets do not have enough time to solidify individually and instead coalesce into a growing macrodrop. Figure 5.3 shows a growing octacosane macrodrop being continuously fed by a high-frequency stream of microdrops. The macrodrop spreads on the target and the contact line arrests early, then the drop grows on its arrested base, keeping a spherical cap shape, as it is still being fed by the stream of droplets. The macrodrop grows until delivery stops, and then solidifies at a longer

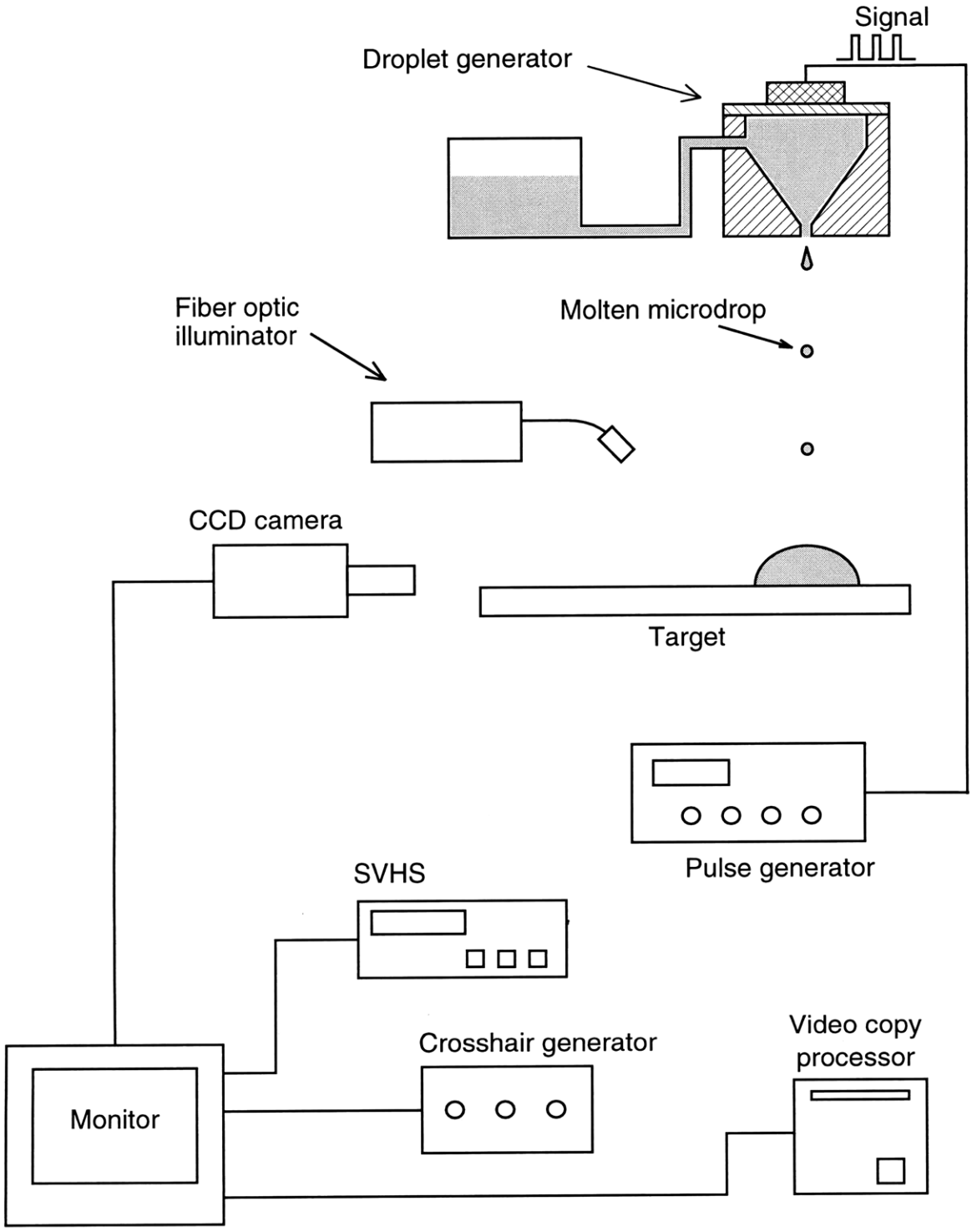

Figure 5.2 Schematic of experimental apparatus for microdrop deposition

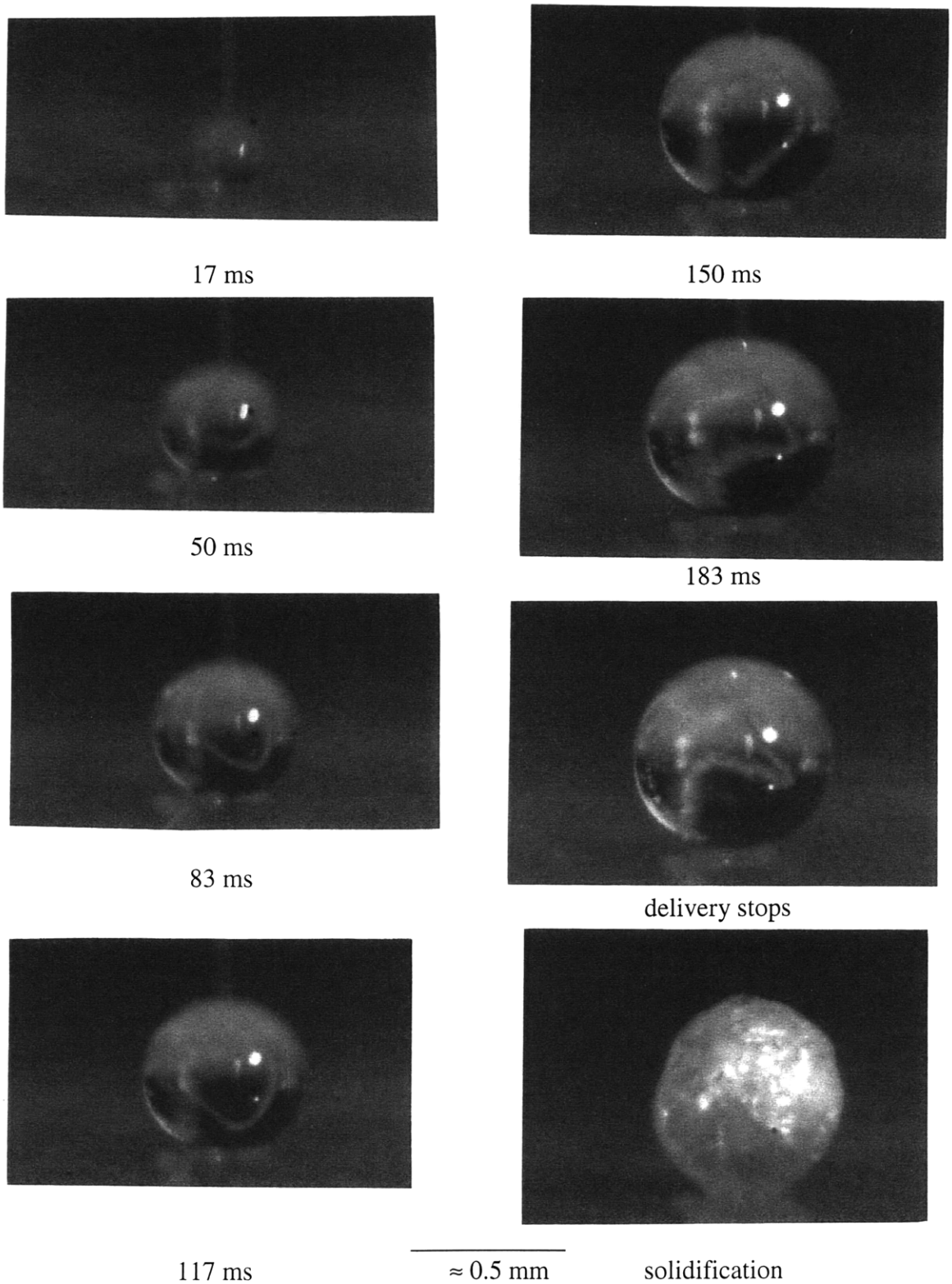

Figure 5.3 Growing Octacosane Macrodrop Spreading on an Octacosane Target. $f = 10$ kHz, $T_o = 78$ °C, $T_t = 53$ °C.

timescale. This technique allows for a more accurate characterization of the spreading process and measurement of the solidification angles.

As a first approach to understanding the deposition process, we conducted a limited study of the solidification angles of molten octacosane deposited on a solid octacosane target. Molten octacosane droplets, approximately 50 μm in diameter, were delivered to the target at a frequency of 10 kHz, where they coalesced forming a macrodrop. The deposition process was recorded and the final solidification angle of the macrodrop was measured. The only experimental parameters that were varied were the number of microdrops deposited, N, and the target temperature, T_t. The number of droplets deposited determined the size of the macrodrop, as well as the time of deposition, since the deposition frequency, f, was unchanged. The temperature of the nozzles, T_o = 78 °C, was also kept constant in the experiments. The fusion temperature of octacosane, T_f, is 61 °C.

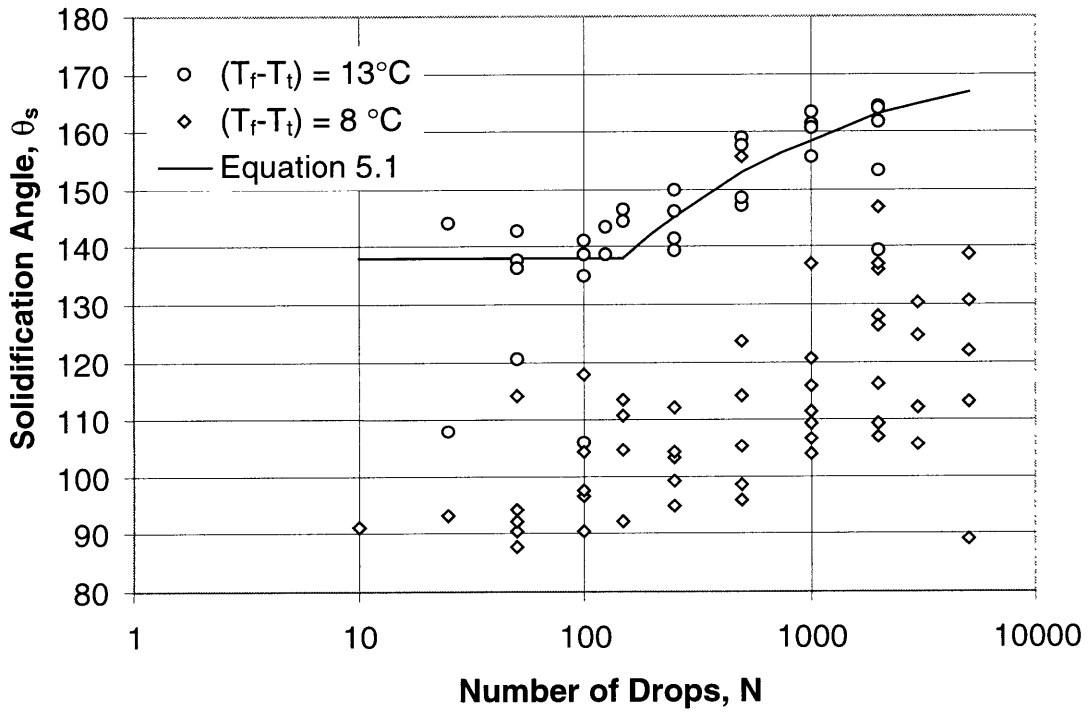

Figure 5.4 Solidification Angle against Number of Drops Deposited. f = 10 kHz, (T_o-T_f) = 17 °C

Figure 5.4 shows the solidification angle as a function of the number of microdrops delivered, for two different values for the target subcooling, T_f-T_t, 13 °C and 8 °C. It is apparent that a higher target temperature results in lower solidification angles. Bringing the target temperature closer to the material's melting point lowers the heat transfer rate and therefore allows the macrodrop to spread further before arresting. If the macrodrop size is kept constant, a larger base radius (radius of the arrested contact line) results in a lower solidification angle. It is an interesting result that the solidification angles were mostly above 90°, even for target temperatures close to the melting point of octacosane, 61 °C.

With regards to the solidification angle as a function of the number of microdrops deposited, the octacosane experimental results were somewhat different from the results obtained by Gao (1994) and Schiaffino (1996) using candelilla and microcrystalline wax, respectively. The previous work showed that the solidification angle as a function of the number of drops, N, has two identifiable regimes. In the first regime, the solidification angle is independent of N. This is valid at lower values of N, where delivery stops before the contact line arrests. In the second regime, characterized by droplet delivery after arrest, the solidification angle increases with N, since the contact line is frozen in place while the mostly liquid macrodrop grows and bulges out over its arrested base. The transition between the two regimes is sharp, and occurs at N^*, the point of contact line arrest.

In Figure 5.4, it appears that the solidification angles at a target subcooling of 13 °C (T_t = 48 °C) follow the pattern observed by Gao and Schiaffino. The transition occurs approximately at N^*=150. When N<150, the solidification angle appears to be constant, about 138 °. As N increases above 150, θ_s increases as given by mass conservation of a macrodrop growing over its arrested base:

$$\frac{R_b^{*3}}{Na^3} = \frac{4\sin\theta_s(1+\cos\theta_s)}{(1-\cos\theta_s)(2+\cos\theta_s)}, \tag{5.1}$$

where a is the radius of each microdrop (≈25μm) and R_b^* is the arrested base radius. R_b^* can be obtained by substituting the values of N^* and the apparently constant θ_s below N^* in Equation 5.1.

For the solidification angles at a target subcooling of 8 °C (T_t=53 °C), however, it is not possible to identify two different regimes from the data, and the scatter in the data is very large, spanning up to 40° for the same experimental conditions. The trend shown by our experiments at this target temperature is that the solidification angles generally increase with increasing number of droplets deposited. The departure from the previous pattern and the large scatter might be related at least in part to an observed phenomenon during the spreading process: periodic droplet "collapse".

Dynamic collapse of a growing, arrested drop was first observed by Gao (1994), while depositing large candelilla wax macrodrops on a Plexiglas target. Figure 5.5 shows an example of this phenomenon. After the contact line arrests, the macrodrop grows and bulges out as it is fed by the microdrop stream. However, at some point the drop collapses, suddenly spreading over the target, and the contact line reaches a new arrest position. The collapse process occurs faster than 16.7 ms, the time interval between frames on the CCD camera.

This phenomenon was very common in our octacosane experiments, often occurring more than once during the deposition of a single macrodrop. If the phenomenon takes place, the final solidification contact angle is highly dependent on both the time when the contact line jumps, and how far it moves. Unfortunately, droplet collapse is apparently not a very repeatable phenomenon, which accounts for the large scatter of the data in Figure 5.4. This phenomenon occurred less frequently at the target temperature of 48 °C than at 53 °C, which suggests a correlation with warmer targets.

Droplet collapse may be caused by remelting of the frozen contact line. After the contact line first freezes, superheated melt is added to the macrodrop. Since the bulk of the macrodrop is still molten, this melt circulates close to the frozen contact line, especially when the contact angle is large. The contact line may eventually remelt, jumping to a new position and refreezing.

The presence of droplet collapse makes it difficult to analyze and interpret the solidification angle data. Further work is needed to determine exactly what causes the phenomenon and why it is not repeatable. It is also desired to learn more about the early stages of the spreading of octacosane macrodrops. This can be achieved by using a high-speed camera to record the deposition process. The present study of octacosane

solidification contact angles can be expanded by varying other deposition parameters, i.e. the frequency of deposition and the initial temperature of the microdrops.

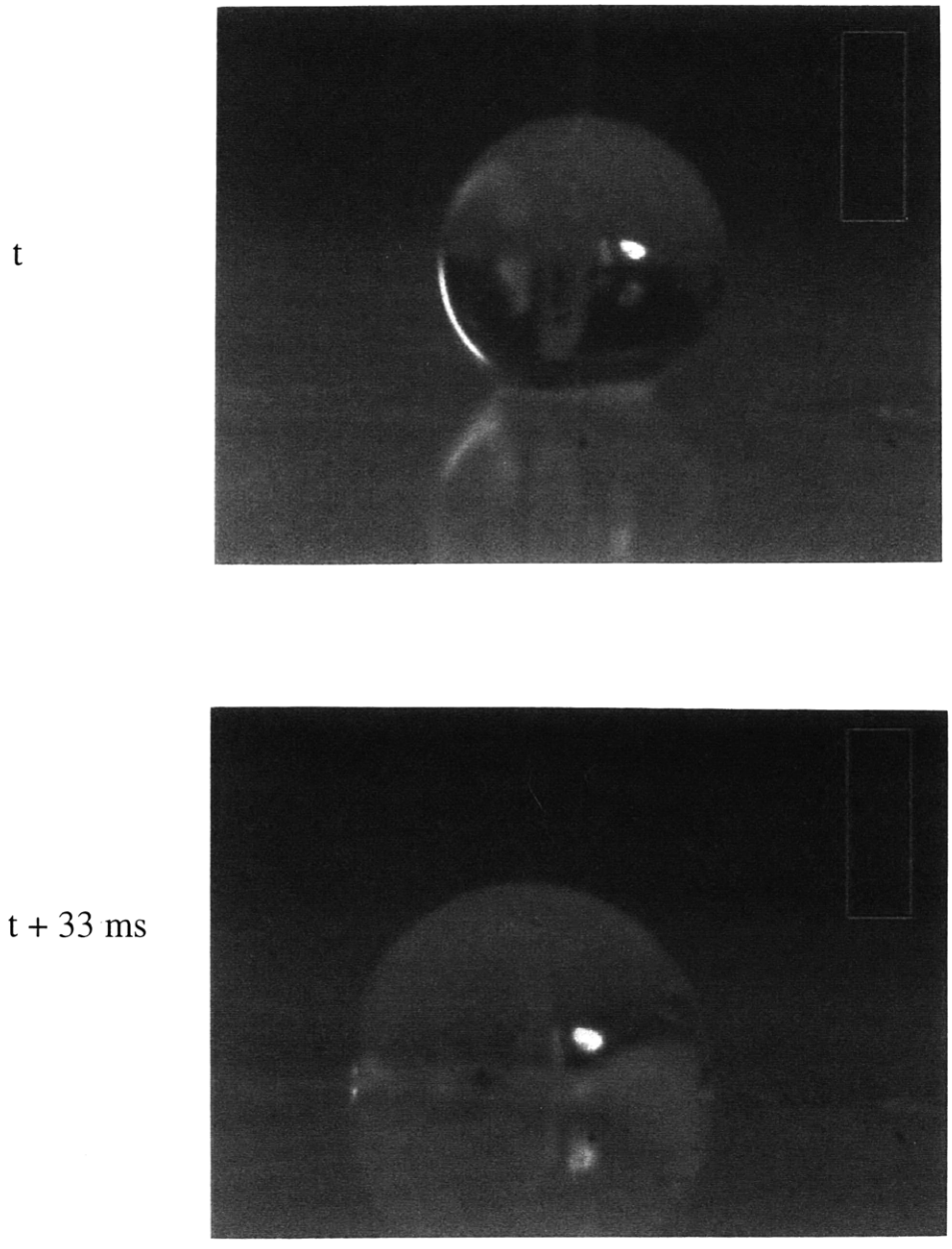

Figure 5.5 Dynamic Collapse of an Octacosane Macrodrop. f=10 kHz, T_o=78°C, T_t=53°C.

Chapter 6
CONCLUSIONS

Previous researchers in this laboratory have investigated the fundamentals of an innovative method for microfabrication by molten microdrop deposition and solidification (Gao ,1994; Gao and Sonin, 1994; Schiaffino, 1996; Schiaffino and Sonin, 1997a-d). Part of their work has attempted to characterize the motion and arrest of a molten material over a subcooled target by performing experiments with candelilla and microcrystalline waxes. In order to have a better understanding of the deposition process, it is necessary to measure the solidification properties of the materials used in deposition and to study the effect of the properties on the solidification process. We limited our study to two materials: microcrystalline wax and octacosane, a long-chain paraffin.

The first task was to measure the enthalpy and specific heat of microcrystalline wax at temperatures between 0 °C and 115 °C. Calorimetric experiments performed in a thermos indicate that, between 30 °C and 90 °C the wax goes through a transition zone, where latent heat is released as it cools. In the solid state below 30 °C, the specific heat of wax was 2000 ± 10% J/kg K. The liquid state above 90 °C showed a higher specific heat, about 2900 ± 5% J/kg K. The latent heat released between 90 °C and 30 °C, taking 2000 J/kg K as the baseline specific heat, is 190 ± 5% kJ/kg.

The next step was to devise a method of measuring the thermal conductivity of microcrystalline wax, and to establish a model for characterizing its solidification. We designed an apparatus to measure the temperature history of microcrystalline wax under one-dimensional transient solidification. We then modeled the solidification process and solved it numerically, iteratively finding a value for the thermal conductivity that made the model agree with the experimental data. The value obtained for the thermal conductivity was 0.073 ± 30% W/m K. We conclude that the model accurately characterizes the solidification of microcrystalline wax.

Next, we conducted a general theoretical investigation of solidification of materials that, like wax, release latent heat over a temperature range. One of the findings of this investigation is that, if the cold temperature at the boundary is constant, the position of the solidification front is directly proportional to the square root of $\alpha_o t$, where

α_o is a reference thermal diffusivity and t is the time. To determine the exact position of the solidification front, however, we need to compute the value of λ, a dimensionless "solidification coefficient". This solidification coefficient is a function of the Stefan number, S, the melt superheat, β, and the ratio between the size of the latent heat transition zone, ΔT, and the subcooling (T_f-T_c). The functional relationship between the solidification coefficient and the parameters it depends on was determined numerically, providing interesting results. One of these is that for a given material, if ΔT is of the same order or larger than the subcooling, then λ has a very weak dependence on parameters other than the superheat, β.

Finally, we studied the spreading and solidification of molten octacosane droplets on a solid target of the same kind. We looked in particular at the solidification angles of molten octacosane macrodrops. We found that the solidification angles were quite large, mostly above 90°, even at a target temperature just 8 °C below the melting point of octacosane. The experiments showed, as expected, that target temperatures closer to the melting point of the material result in smaller solidification angles. If the target temperature and frequency of deposition are held constant, then a larger number of droplets deposited generally results in larger angles. However, the analysis and interpretation of the data was difficult due to a large scatter in the data. This large scatter might have been caused by droplet collapse, an irregular, unpredictable phenomenon that was observed during deposition. Further work is needed to investigate the nature of this phenomenon, where the contact line, after being frozen for some time, suddenly jumps and reaches a new arrested position. One possibility is that the contact line remelts due to the hot liquid above it. In any case, additional work is needed in this area to properly characterize the spreading and arrest of octacosane droplets.

NOMENCLATURE

a	microdrop radius
c	specific heat
c_o	specific heat of a material outside of the melting transition region (Chapter 4)
C_t	heat capacity of thermos
ΔH	enthalpy change
ΔH^*	adjusted enthalpy change
k	thermal conductivity
L	latent heat
m	mass
N	number of droplets
N^*	number of droplets at which the contact line freezes
Q_{12}	heat loss to ambient
R_b^*	contact line radius after solidification
S	Stefan number
T	temperature
T_1	initial temperature of water inside the thermos
T_2	initial wax temperature
T_3	initial temperature of water outside the thermos
T_c	cold boundary temperature
T_e	equilibrium temperature
T_f	fusion temperature
T_o	initial melt temperature
T_t	target temperature
T_{ref}	reference temperature
ΔT	size of the temperature range over which latent heat is released
x	position
x_s	position of the solidification front

Greek symbols

α	thermal diffusivity
β	melt superheat
θ_s	solidification angle
λ	solidification coefficient
ρ	density

REFERENCES

Carslaw, H. S. and Jaeger, J.C., 1959, *Conduction of Heat in Solids*, Oxford, New York.

Daubert, T. E. and Danner, R. P., 1989, *Physical and Thermodynamic Properties of Pure Chemicals: Data Compilation,* Hemisphere, New York.

Domalski, E. S., Evans W. H., and Hearing E. D., 1984, *Heat Capacities and Entropies of Organic Compounds in the Condensed Phase,* American Chemical Society, Washington, D.C.

Gao, F.,1994, Molten Microdrop Deposition and Solidification Processes, Ph.D. Thesis, Department of Mechanical Engineering, MIT.

Gao, F. and Sonin, A. A., 1994, Precise Deposition of Molten Microdrops: the Physics of Digital Microfabrication, *Proc. Roy. Soc. London A*, **444**, 533-554.

Garcia, A. and Prates, M., 1978, Mathematical Model for the Unidirectional Solidification of Metals: I. Cooled Molds, *Metallurgical Transactions*, **9B**, 449-457.

Landolt-Bornstein, 1995a, New Series, GroupIV, Vol. 8A, Springer-Verlag, Berlin.

Landolt-Bornstein, 1995b, New Series, GroupIV, Vol. 8B, Springer-Verlag, Berlin.

Lipton, J., Garcia, A., and Heinemann, 1982, An analytical solution of directional solidification with mushy zone, *Archiv fur das Eisenhuttenwesen*, **53**, 469-473.

Mathot, V., 1994, *Calorimetry and Thermal Analysis of Polymers*, Hanser, New York.

Reed Wax, Reading, MA, *Specifications*.

Schiaffino, S., 1996, The Fundamentals of Molten Microdrop Deposition and Solidification, Ph.D. Thesis, Department of Mechanical Engineering, MIT.

Schiaffino, S. and Sonin, A.A., 1997a, Formation and Stability of Liquid and Molten Beads on a Solid Surface, *J. Fluid Mech.*, **343**, 95-110.

Schiaffino, S. and Sonin, A.A., 1997b, Motion and Arrest of a Molten Contact Line on a Cold Surface: an Experimental Study, *Phys. Fluids*, **9**, 2217-2226.

Schiaffino, S. and Sonin, A.A., 1997c, On the Theory for the Arrest of an Advancing Molten Contact Line on a Cold Solid of the Same Material, *Phys. Fluids*, **9**, 2227-2233.

Schiaffino, S. and Sonin, A.A., 1997d, Molten Droplet Deposition and Solidification at Low Weber Numbers, *Phys. Fluids*, **9**, 3172-3187.

Warth, A. H., 1956, *The Chemistry and Technology of Waxes*, 2nd ed., Reinhold, New York.

Wendlandt, W. W., 1986, *Thermal Analysis*, 3rd ed., John Wiley and Sons, New York.

Appendix A

POSITION OF THE SOLIDIFICATION FRONT IN MATERIALS WITH TEMPERATURE-DEPENDENT SPECIFIC HEAT

In Chapter 4, we dealt with the problem of one-dimensional solidification of a semi-infinite body that releases latent heat over a temperature range. As part of our theoretical analysis, we stated that the position of the solidification front, x_s, had the form

$$x_s = \lambda\sqrt{\alpha_o t}\,, \tag{A.1}$$

where

$$\alpha_o = \frac{k}{\rho c_o}\,, \tag{A.2}$$

and c_o is given in Figure 4.1. In this Appendix, we conduct a dimensional analysis that shows that Equation A.1 holds true even for materials with a temperature-dependent specific heat.

The energy equation and boundary conditions that solve our transient solidification problem (Equations 4.8 and 4.9) can be written as

$$\frac{1}{\alpha(T-T_f)}\cdot\frac{\partial(T-T_f)}{\partial t} = \frac{\partial^2(T-T_f)}{\partial x^2}\,,$$

$$\begin{aligned} &x = 0: \quad T - T_f = -(T_f - T_c)\,, \\ &x \rightarrow \infty: \quad T - T_f = T_o - T_f\,, \\ &t = 0: \quad T - T_f = T_o - T_f\,, \end{aligned} \tag{A.3}$$

where α is the temperature-dependent thermal diffusivity, T_f is the melting temperature, t represents the time, T_o is the initial temperature of the body, T_c is the cold temperature at the boundary, and x is the distance from the boundary.

For a material with a specific heat curve like the one given in Figure 4.1, the thermal diffusivity can be expressed as

$$\alpha(T-T_f) = \frac{\alpha_o}{1 + 2\left(\frac{L}{c_o}\right)\left(\frac{(T-T_f)+\Delta T}{(\Delta T)^2}\right)}\,, \tag{A.4}$$

where L is the latent heat and ΔT is the size of the melting transition zone, as shown in Figure 4.1.

We now have the complete set of equations and boundary conditions that can be solved to obtain the temperature field as a function of time. By inspection of Equations A.3 and A.4, we can say that for $T_c < T < T_o$,

$$x = x\left(t,(T-T_f),(T_f-T_c),(T_o-T_f),\alpha_o,\frac{L}{c_o},\Delta T \right). \tag{A.5}$$

Since the position of the solidification front is defined as

$$x_s = x\big((T-T_f)=0\big), \tag{A.6}$$

then

$$x_s = x_s\left(t,(T_f-T_c),(T_o-T_f),\alpha_o,\frac{L}{c_o},\Delta T \right). \tag{A.7}$$

The parameters in Equation A.7 have dimensions of length, time and temperature. A dimensional analysis allows us to express Equation A.7 in dimensionless terms:

$$\frac{x_s}{\sqrt{\alpha_o t}} = \lambda\left(\frac{(T_o-T_f)}{(T_f-T_c)},\frac{c_o(T_f-T_c)}{L},\frac{\Delta T}{(T_f-T_c)} \right), \tag{A.8}$$

obtaining precisely Equation A.1.

Recognizing that the first two parameters on the right side of Equation A.8 are the superheat, β, and the Stefan number, S, we rewrite the expression to get

$$\frac{x_s}{\sqrt{\alpha_o t}} = \lambda\left(\beta,S,\frac{\Delta T}{(T_f-T_c)} \right), \tag{A.9}$$

as expressed previously by Equation 4.7.

Appendix B

THERMO-PHYSICAL PROPERTIES OF MICROCRYSTALLINE WAX AND OCTACOSANE

Property	Microcrystalline wax	Octacosane
Melting point (°C)	90 (b)	61.4 (f)
Solid-solid transition point (°C)	N/A	58.1 (f)
Solid density (kg/m^3)	930 (20 °C) (a)	804 (22.5 °C) (g)
Liquid density (kg/m^3)	780 (95 °C) (a)	774 (70 °C) (g)
Viscosity (mPa s)	17 (95 °C) (b)	4.9 (70 °C) (h)
Surface tension (N/m)	0.025 (c)	0.026 (h)
Thermal conductivity (W/m K)	0.073 (d)	0.15 (h)
Specific heat (J/kg K)	2000 (20 °C), 2900 (95 °C) (e)	2378 (80 °C) (i)
Latent heat (kJ/kg)	190 from 30°C - 90°C (e)	163.6 @61.4 °C (f)
Heat of transition (kJ/kg)	N/A	89.8 @58 .1 °C (f)

Sources:

(a) Reed Wax.

(b) Schiaffino (1996).

(c) Gao (1994).

(d) Chapter 3.

(e) Chapter 2.

(f) Landolt-Bornstein (1995a).

(g) Landolt-Bornstein (1995b).

(h) Daubert and Danner (1989).

(i) Domalski et al. (1984).

Appendix C

ERROR ANALYSIS FOR ENTHALPY EXPERIMENT

The measurement of the enthalpy of microcrystalline wax at different temperatures depended on the accurate measurement of several sub-quantities that determine the enthalpy. These include the mass of the wax and the water, the initial and final temperatures, and the heat capacity of the thermos. In order to estimate the error of the enthalpy measurement, we need to know how the error of each individual quantity affects the overall error.

In general, if

$$f = f(x_1, x_2, ..., x_n) \tag{C.1}$$

then a conservative estimate of the error involved in calculating f is

$$e_f = e_{x_1} \frac{\partial f}{\partial x_1} + e_{x_2} \frac{\partial f}{\partial x_2} + ... + e_{xn} \frac{\partial f}{\partial x_n} , \tag{C.2}$$

where e_i is the error of the variable i.

In our case, the enthalpy change of the wax from the reference temperature to a temperature T_2 is calculated by Equation 2.4, along with either Equation 2.2 or 2.3. The error of each of the variables in the equations can be estimated according to the accuracy of the measurement device or the data source. For instance, the temperature measurements were taken to be accurate to ± 0.2 °C, the mass measurements to ± 0.1 g, and the specific heat of water to ± 1%. The error in the measurement of the heat capacity of the thermos, C_t, was estimated at ± 15%, using a separate error analysis of Equation 2.1.

After the error of each of the variables was estimated, the overall error of each enthalpy data point was determined independently according to Equation C.2. In this analysis, it was found that the major sources of error were the temperature measurements, accounting for about 2/3 of the overall error, and the heat capacity of the thermos (≈1/3 of the overall error). The magnitude of the overall error itself is different for each data point. For temperatures above 60 °C, the error in the enthalpy is approximately ± 5%, between 40-60 °C, about ± 7.5%, and below 40 °C, ±10%.

Appendix D

DATA

Table D.1 Data for Figure 2.2

Heat Capacity of the Thermos vs. Final Mass of Water Inside

Final Mass of Water Inside the Thermos (kg)	Heat Capacity of the Thermos (kJ/K)
0.128	88
0.2132	103.1
0.3433	132.2
0.6291	182.3

Table D.2 Data for Figure 2.3

Enthalpy Change of Wax vs. Temperature

Initial Wax Temperature (°C)	Enthalpy Change (kJ/kg)
2.6	-22
13.5	0
38	49
40.4	61.2
44.5	84.6
50	100.3
56	118
60	138
65	168.4
70	187.5
75	223
80	256
84.5	295
90	342.3
93	350.6
95	353.3
105	388
110	400
115	412.3

Table D.3 Data for Figure 3.2

Thermal Conductivity of Wax vs. Distance between Thermocouple and Copper Plate

Thermocouple Distance (mm)	Thermal Conductivity (W/m K)
4.5	0.072
5.5	0.063
6	0.08
6	0.056
6.5	0.07
6.5	0.061
8	0.06
9	0.086
9	0.086
9.5	0.082
10.5	0.079
11	0.08

Table D.4 Data for Figure 3.3

Position of the Solidification Front, x_s as a Function of Time

Time (s)	x_s (mm)
0	0
163	4.5
250	6
405	8

Table D.5 Data for Figure 3.4

Temperature History for Different Thermocouple Heights

4.5 mm		6 mm		8 mm	
Time (s)	Temp. (C)	Time (s)	Temp. (C)	Time (s)	Temp. (C)
0	92.7	0	92.7	0	92.7
120	91	190	91	259	91.5
163	90	250	90	362	90.5
220	88.5	333	88.5	405	90
295	86.5	396	87.5	465	89.5
350	85	468	86	583	88
431	83	524	85	625	87.5
509	81				

Table D.6 Data for Figure 5.4

Solidification Angle, θ_s vs. Number of Drops Deposited, N. f = 10 kHz, $(T_o - T_f)$ = 17 °C

$(T_f - T_t)$ = 8 °C		$(T_f - T_t)$ = 13 °C	
N	θ_s	**N**	θ_s
10	78.8	25	108.0
10	91.3	25	144.2
25	93.3	50	120.6
25	93.3	50	137.9
25	178.3	50	142.9
50	90.5	50	136.3
50	94.2	100	106.0
50	178.4	100	135.0
50	87.6	100	141.3
50	114.0	100	138.7
50	87.6	125	138.7
50	92.1	125	143.4
100	96.5	150	146.7
100	93.3	150	144.5
100	78.8	250	149.8
100	117.9	250	146.3
100	97.5	250	141.4
100	90.3	250	139.5
100	104.5	500	159.0
100	117.9	500	157.7
150	113.5	500	147.3
150	104.6	500	148.7
150	110.6	1000	161.5
150	92.3	1000	163.5
250	103.3	1000	163.5
250	94.8	1000	155.6
250	94.2	1000	160.9
250	93.3	2000	153.2
250	99.3	2000	164.6
250	112.0	2000	139.5
250	104.5	2000	164.1
250	104.5	2000	161.6
500	98.6		
500	105.3		
500	105.3		

$(T_f-T_t) = 8$ °C	
N	θ_s
500	96.5
500	90.5
500	155.6
500	123.5
500	114.1
500	114.1
500	96.0
1000	109.3
1000	106.7
1000	104.1
1000	105.3
1000	103.3
1000	94.8
1000	120.4
1000	111.3
1000	137.1
1000	115.9
2000	109.5
2000	116.2
2000	136.2
2000	128.1
2000	178.3
2000	107.0
2000	137.0
2000	126.2
2000	146.9
3000	130.4
3000	112.2
3000	105.6
3000	124.6
5000	113.1
5000	138.7
5000	130.8
5000	89.3
5000	121.7